Int. J. Electrochem. Sci., 14 **(2019)** 2509 – 2525, doi: 10.20964/2019.03.65

International Journal of
ELECTROCHEMICAL
SCIENCE
www.electrochemsci.org

Influences of Thermomechanical Conditions on Corrosion Behavior of low-carbon steels in Artificial Seawater

Dongsheng Wang[1], Qianjin Zhao[2], Ti Yang[2], Xueting Chang[1,], Shaopeng Qu[1], Shibin Sun[2], Shan Gao[3], Caiyi Zhang[3], Xiaohui Lu[3], Yansheng Yin[1]*

[1] College of Ocean science and Engineer, Shanghai Maritime University, Shanghai 200135, China
[2] College of logistics Engineer, Shanghai Maritime University, Shanghai 200135, China.
[3] Research institute of Baosteel Co., Ltd, Shanghai 201900, China.
[*]E-mail: xtchang@shmtu.edu.cn

Received: 11 October 2018 / *Accepted:* 18 December 2018 / *Published:* 7 February 2019

The unprecedented global warming process causes the shrinking of sea ice in the polar region every year; hence, in order to withstand the harsh environment of this region as well as to reduce the transportation cost, a large number of high-strength steels are required to build icebreakers. The main objective of the present study was to investigate the corrosion behavior of both water-quenched and air-cooled low-carbon steels in 3.5% artificial NaCl solution. It was found that after the corrosion of lamellar ferrites in pearlites and martensites, the remaining cementites aggravated the galvanic corrosion and the pitting corrosion in the matrix. Further, dislocation and the presence of large fractions of cementite in the matrix deteriorated the corrosion resistance property of the directly water-quenched sample. However, the air-cooling process significantly improved the corrosion resistance behavior of the sample steel.

Keywords: Corrosion, Electrochemical impedance spectroscopy, Low-temperature carbon steel, Thermomechanical controlled process, Quenching

1. INTRODUCTION

Since 1950, the global climate has been experiencing an unprecedented warming process, thus causing the shrinking of sea ice as well as amplifying the polar region every year [1], and this phenomenon is supposed to accelerate the transition of seasonally open seas. The warming speed of the Arctic is found to be about twice as fast as other regions of the earth; therefore, a continuous monitoring is required to reveal the changing conditions of the polar region. The reprocessing of sea ice in summer opens up new opportunities for polar scientists to explore the once-inaccessible water area of the Arctic.

Business industries are continuously trying to exploit the Arctic for tourism, fishing, shipping, and natural resources. According to the report of the U.S. geological survey [2], the Arctic contains 30% of the total natural gas resource in the world and also 13% of its undiscovered oil. As in the summer, the

level of polar ice shrinks, cargo transport in the Arctic waters increases significantly. Shipping companies have already begun to exploit the Arctic shipping routes as a shortcut to transport cargos between the Pacific rim cities and the Atlantic coastal cities using an increasing number of ice-enhanced vessels.

The temperature of the polar region changes within the range of –70°C to 30°C [3]; hence, in order to withstand the harsh environment of this region as well as to reduce the transportation cost, a large number of high-strength steels are required to build icebreakers, drilling platforms, and machinery [4]. In order build advanced polar vehicles with improved mechanical properties (ductility, high-strength, low-temperature toughness, cold resistance, fracture toughness, weldability, and seawater corrosion resistance), different micro-alloying elements, rolling processes, and heat treatment methods are often employed [5-7]. Thermomechanical controlled process (TMCP) is also widely applied to improve the overall mechanical properties as well as to optimize the crystal structures of marine steel plates [8-12]. Chin-Hyung Lee [13] evaluated the welding performance of TMCP plates in extremely cold areas. The effects of quenching and partitioning on microstructures and mechanical properties of TMCP steels were reported by Parthiban [14], Hu [15], and Wang [16].

Some previous researchers [17-20] applied various heat treatment methods at different cooling speeds to prepare high-strength shipbuilding steels with optimized mechanical properties. Further, some studies [21-22] exploited the potentials of low-carbon steels by using the generated waste heat in hot rolling processes. However, very few works explored the seawater corrosion resistance behavior of low-carbon alloy steels. The main purpose of the present paper was to investigate the corrosion behavior of both water-quenched and air-cooled low-carbon steels in 3.5% artificial NaCl solution under different cooling methods.

2. EXPERIMENTAL PROCEDURES

2.1 Materials

The procured ice-enhanced ship hull low-carbon alloy steel plate was composed of the following chemical elements: C (0.12 wt%), Si (0.99 wt%), Mn (0.63 wt%), Cr (0.76 wt%), Ni (0.66 wt%), Mo (0.11 wt%), Cu (0.47 wt%), and Al (0.027 wt%). After melting in a vacuum induction furnace (R&D center, Bao Steel Co. Ltd.), the steel plate was cast into a steel billet of 250 mm × 250 mm size, and its critical temperature (A_{r3}) was calculated by Thermocalc 5.0 software. The martensite-start (M_s) and the martensite-finish (M_f) temperatures were calculated by the empirical formula reported in the literature [23]. The slab was first austenitized at 1200°C for 1.5 h and then rough milled from 250 to 76 mm thickness through six passes at about 1100°C. The plate was again hot rolled to 30 mm thickness through six passes during air-cooling to 920°C, and the finishing rolling temperature was set to 880°C. The schematic representation of different thermal profiles is illustrated in Fig. 1. Process 1 depicts the air-cooling process of the steel plate after hot rolling, and the sample was marked as AC. Process 2 represents the direct water quenching process after hot rolling, and the sample was termed as DQ.

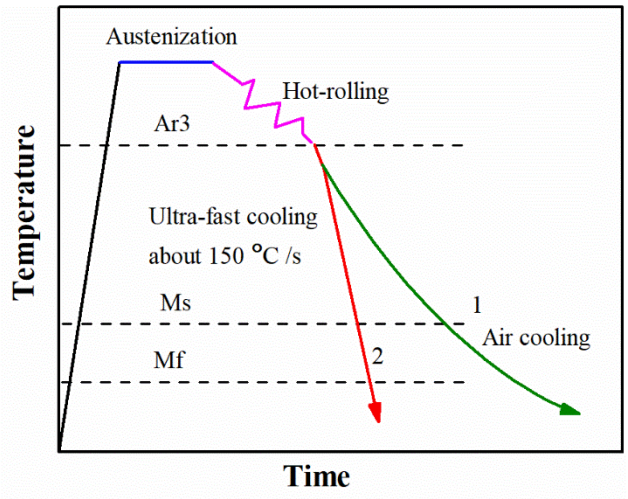

Figure 1. Schematic representation of different thermal profiles of the low-temperature ship steel: 1, air-cooling after hot rolling and 2, direct water quenching after hot rolling

2.2 Weight loss measurements

Corrosion specimens of 50 mm × 25 mm × 2 mm size were cut from both DQ and AC samples. The samples were first grounded by a 1200 mesh SiC paper, then polished by a diamond polisher to remove decarburized layers and scratches on their surfaces, and finally, washed by deionized water and dried in cold air. All samples were immersed vertically (all faces were exposed) into 3.5% saturated sodium chloride (NaCl) solution for 24, 96, 168, and 336 h. After being immersed for different time periods, four specimens were taken out from the solution, and three of them were treated by a de-corroding solution (prepared with hydrochloric acid, deionized water, and hexamethylenetetramine in the proportion of 25:25:1) for 60 s [24]. After removing all corrosion products, the samples were washed and dried in cold air. Each sample was weighed three times, and their average value was considered to calculate the actual mass. The remaining samples were used for surface morphology.

2.3. Electrochemical measurements

The plates (10 mm × 10 mm × 2 mm) for electrochemical experiments were cut from both DQ and AC samples. The electrochemical experiments were carried out in an EZstat-Pro (NuVant Systems Inc.) potentiostat with a three-electrode system. After being sealed by epoxy and polished with a 1200 mesh SiC paper, the samples with an exposed area of 1 cm^2 were set as the working electrode (WE), whereas saturated calomel and saturated calomel electrode (SCE) were used as the reference electrode. The potentiodynamic polarization curves (E, V/SCE) were swept from –1.0 V/SCE to 1.0 V/SCE, and the potential scan rate was set to 0.5 mVs^{-1}. The corrosion current densities and the anode/cathode polarization slopes of the samples were obtained by the Tafel extrapolation method [25]. Electrochemical impedance spectroscopy (EIS) (frequency range of 100–0.01 kHz and potential amplitude of ±10 mV) was performed after the system reached a steady state, and the tested results and the equivalent circuit were fitted by ZsimpWin software. Triplicate tests were executed to verify the accuracies of the obtained

EIS curves.

2.4. Surface characterization of corrosion products

The specimens for microstructural analysis were first grounded and polished and then etched with 4% Nital for 15 s. The morphologies of the samples were observed by a scanning electron microscope (SEM) equipped with an energy dispersive spectrometer (EDS) system at an operating voltage of 10 kV. The area fractions of martensites and pearlites and the average grain size were measured by both quantitatively metallographic analysis and intercept method [26]. Transmission electron microscopy (TEM) at an operating voltage of 200 kV was also carried out to observe the microscopic morphologies of the samples. The TEM specimens were first grounded to a thickness of 45 μm and then electro-polished at –20°C in a twin-jet machine. Further, the XRD analysis of the samples was performed under a Cu-K_α radiation source at a voltage of 40 kV. The scanning speed and the 2θ range for XRD analysis were respectively set to 0.02°/s and 10°–90°.

3. RESULTS AND DISCUSSION

3.1 Surface microstructural characterization

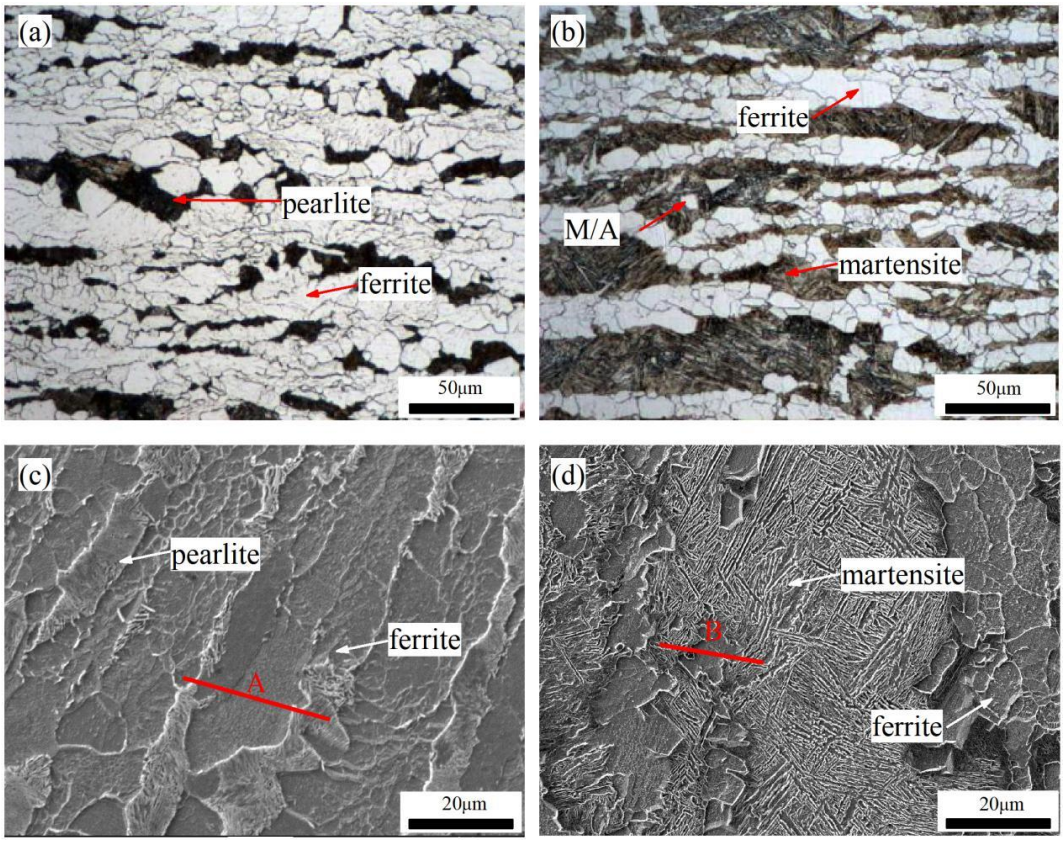

Figure 2. Microstructures of the samples at different cooling speeds: (a)–(c) air cooling after hot rolling and (b)–(d) direct water quenching after hot rolling

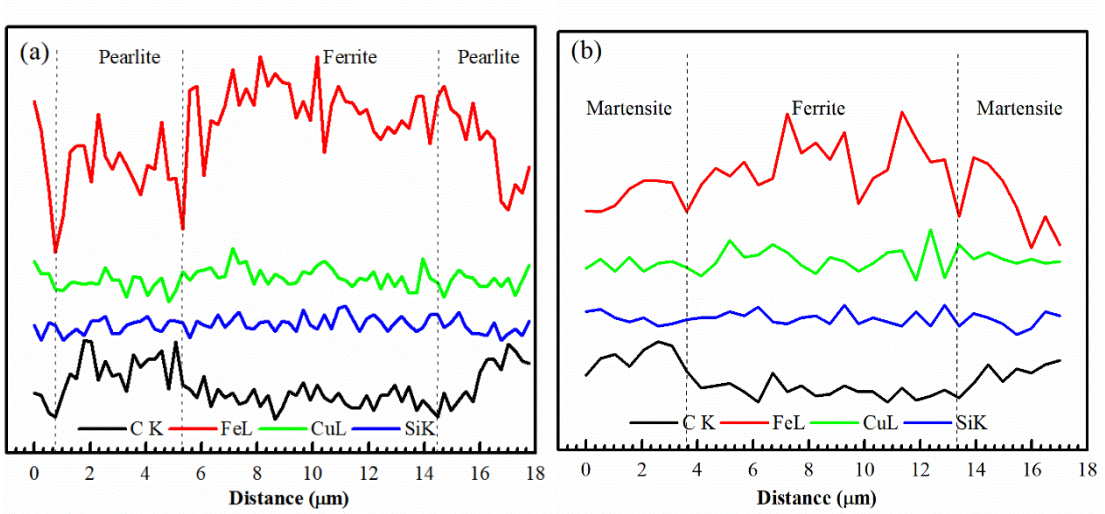

Figure 3. Line profiles (measured by line scanning method) of selected areas in Fig. 2: (a) Line A represents the air-cooled low-carbon steel displayed in Fig. 2(c). (b) Line B represents the directly water-quenched low-carbon steel exhibited in Fig. 2(d)

The microstructures of both water-quenched and air-cooled low-carbon steels at different cooling speeds are exhibited in Fig. 2. The microstructures of the air-cooled samples mainly consisted of polygonal pro-eutectoid ferrites and pearlites, and their grain boundaries were aligned along the rolling direction (Figs. 2(a) and 2(c)). Moreover, the fraction of pearlites and the average ferrite grain size were calculated as about 20% and 17.6 μm, respectively. However, the metallographic structures of the directly water-quenched samples were dominated by ferrites and martensites, and the fraction of martensites was found as 34.7% ((Figs. 2(b) and 2(d)). It was observed that due to both low-carbon content and lower rolling temperature (880°C) than the austenitic transformation temperature, a large number of austenites started to transform into ferrite.

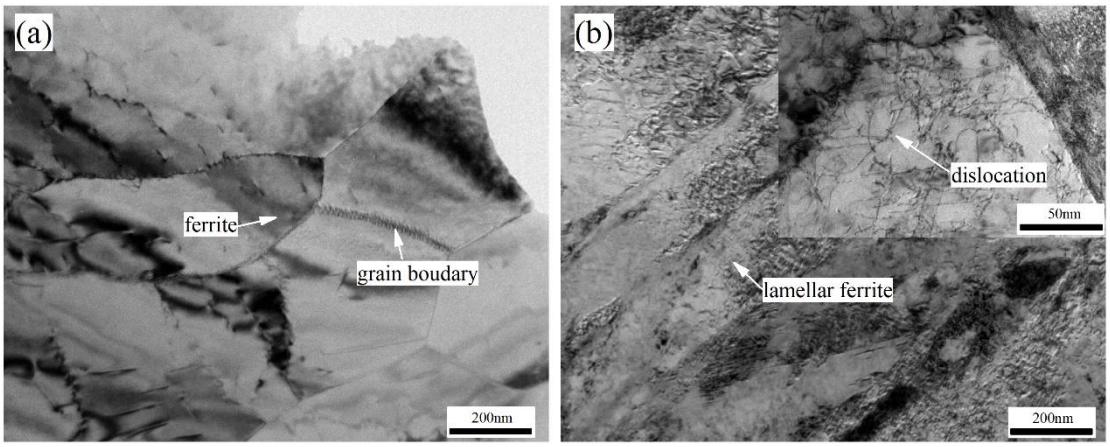

Figure 4. TEM micrographs of the samples for different immersion times in NaCl solution: (a) air cooling after hot rolling and (b) direct water quenching after hot rolling

During water quenching, some unconverted austenites transformed into martensites. It was noticed that due to cementite diffusion, the distribution of carbon in different phases was also differed significantly (Fig. 3). The amount of Fe was found to be the highest in the ferrite phase, whereas pearlite and martensite phases manifested a significant increase in carbon content. The pro-eutectoid ferrite and pearlitic structures are displayed in Fig. 4(a). It is evident that rapid cooling of water-quenched samples led to residual internal stresses and dislocations along grain boundaries (Fig. 4(b)), thus resulting in lower substrate corrosion resistance [27].

3.2 Gravimetry

The weight loss curves of both AC and DQ specimens against immersion time are displayed in Fig. 5(a). It is clear that both samples manifested a similar weight loss trend, and their weight loss values increased with the prolonged immersion times. The weight loss values of directly quenched plates were found to be higher than those of air-cooled steel plates. After 336 h, the weight loss values of AC and DQ samples were calculated as 36.5 and 54.1 mg/cm^2, respectively. It was observed that after an immersion period of 96 h, the weight loss speeds of both samples started to increase rapidly; however, after 168 h, the slopes of the weight loss curves decreased gradually.

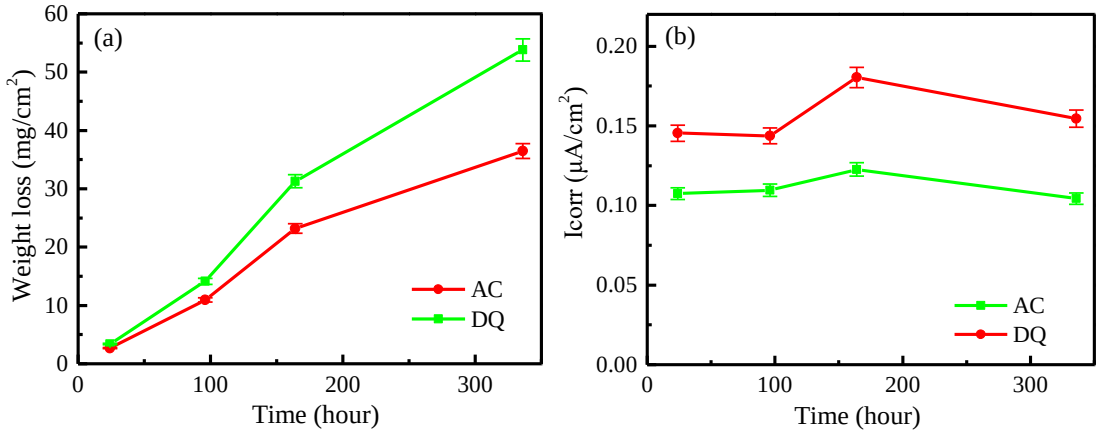

Figure 5. Variations in (a) weight loss (Δm) and (b) instantaneous corrosion current density (I_{corr}*) of AC and DQ specimens for different immersion times

The weight loss data was converted into corrosion current density (I_{corr}) values according to Faraday's law [28]:

$$I_{corr*} = \frac{\Delta m \nu F}{3600 t M} \times 10^6. \quad (1)$$

In Equation (1), as a Fe/Fe^{2+} electrochemical reaction, the values of ν (valency of Fe), F (Faraday constant), and M (molar mass of Fe) were considered as 2, 96485 C/mol, and 56 g/mol, respectively. It is observable from Fig. 5(b) that the I_{corr} values of DQ samples were higher than those of AC plates. The I_{corr} values of DQ plates changed slowly at the beginning and reached a peak of 0.18 μA/cm^2 after 96 h of immersion. Finally, due to the accumulation of corrosion products on sample surfaces, the I_{corr} values

started to decrease gradually. However, for air-cooled plates, the variation in current amplitude was very small and the value of peak corrosion current density was calculated as 0.12 μA/cm^2.

3.3 Electrochemical characteristics

In order to further explain the corrosion mechanism of DQ and AC samples, their electrochemical characteristics before and after immersion in NaCl solution were measured by potentiodynamic polarization measurements (Figs. 6(a) and 6(b)). By comparing the two sets of curves, the passivation zone was found before the samples were immersed in the solution.

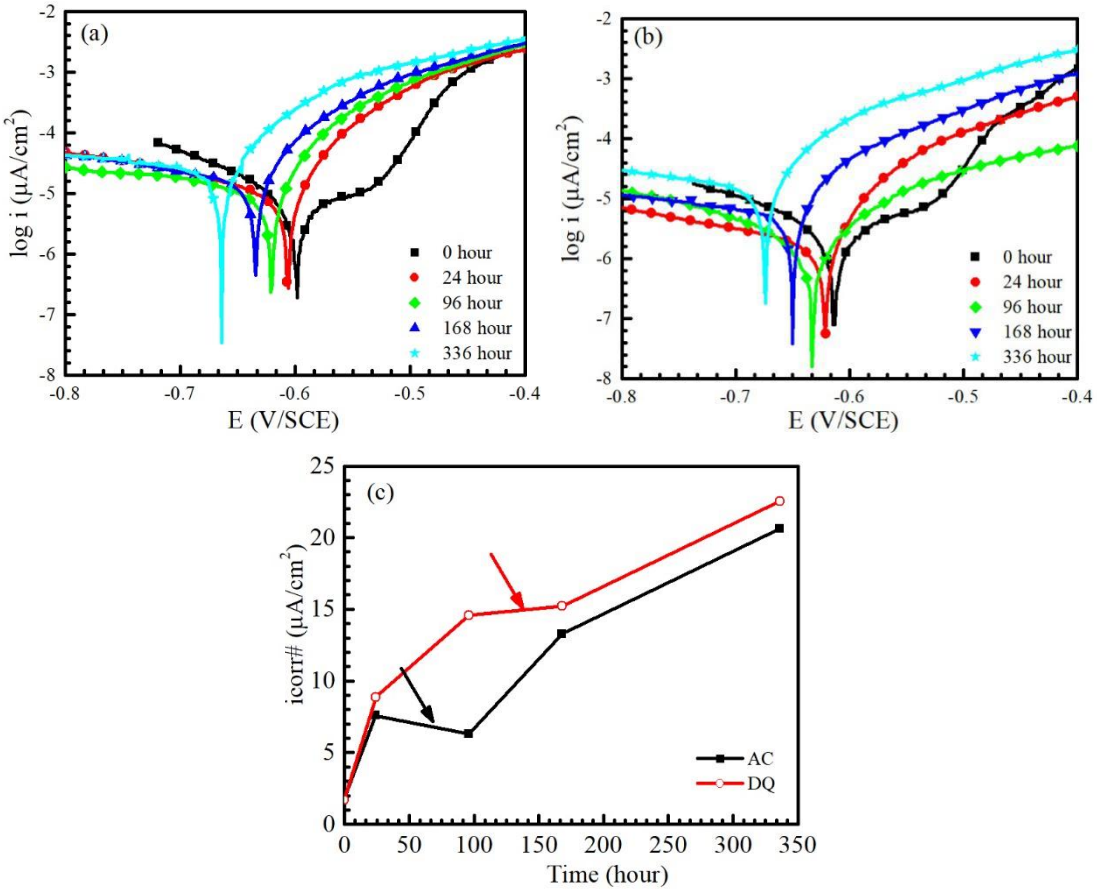

Figure 6. (a) Polarization curves of air-cooled steel samples, (b) polarization curves of directly water-quenched steel samples, and (c) corrosion current densities (calculated by Tafel extrapolation) of AC and DQ samples

During corrosion process, both DQ and AC steel plates experienced the dissolution of ferrite phase on the anode. The inceptive corrosion potential (E_{corr}) values of DQ samples were found to be lower than those of AC steels. Further, due to the constant corrosive reaction, the E_{corr} curves started to shift toward left with the prolonged immersion time. The values of corrosion currents density ($i_{corr\#}$), corrosion potential (E_{corr}), cathodic Tafel slope (β_c), and anodic Tafel slopes (β_a) are presented in Table.1.

Fig. 6(c) displays the variations in corrosion current ($i_{corr\#}$) against immersion time. The $i_{corr\#}$ was low initially, then the corrosion current increases quickly. With the prolongation of immersion time, the

slope of $i_{corr\#}$ decreases gradually. The variation of the corrosion current as the red arrow showed in the Fig. 6(c) is named as "reverse phenomenon", which is often observed during the corrosion process of low carbon steel in marine environment [29]. The cycle of directly quenching samples occurred this phenomenon was later than the air-cooling samples. The corrosion current density values obtained from the electrochemical polarization curves were found to be higher than those calculated from the weight loss curves, due to the accumulation of corrosion products on sample surfaces in different states. The weight loss tested samples were in a static state, and the sample corrosion products on the surface cannot be peeled off in time, and the corrosion products prevented the corrosion reaction from proceeding further. When the corrosion current were caculated, only the weight loss of sample were converted, the effects of other electrochemical reactions occurred during electron migration was ignored. The surface of the sample using the potentiodynamic polarization method to measure the surface corrosion current was treated instantaneously by contrary. The deviation in corrosion current densities calculated by potentiodynamic polarization method and natural corrosion method increased with the prolonged immersion time. Therefore, the former method can be used to measure the general macroscopic corrosion trend of AC and DQ steels, whereas the latter could be employed to explore the corrosion mechanism of the tested samples.

Table 1. Electrochemical kinetic parameters for the Tafel extrapolation curves used in Fig. 6(C)

Specimen	$I_{corr\#}$(μA/cm^2)	E_{corr}(V/SCE)	-β_c (mV/dec)	β_a (mV/dec)	Corrosion rate (10^{-3}mm/y)
AC-0 h	1.67	–0.60	90.9	185.7	1.16
AC-24 h	7.75	–0.61	228.2	46.7	5.25
AC-96 h	6.29	–0.62	773.4	55.4	10.10
AC-168 h	13.273	–0.63	283.1	48.0	9.19
AC-336 h	20.63	–0.66	416.2	58.2	14.99
DQ-0 h	1.85	–0.62	89.1	121.6	1.28
DQ-24 h	8.86	–0.62	245.6	41.3	7.14
DQ-96 h	14.56	–0.63	203.1	109.1	9.59
DQ-168 h	15.24	–0.65	361.6	48.9	10.57
DQ-336 h	22.51	–0.68	395.5	58.0	15.60

The electrochemical impedance curves under open circuit potential were used to evaluate the influences of corrosion products on corrosion mechanism of AC and DQ steels. Fig. 7 illustrates the Nyquist curves and the bode phase/angle vs frequency diagrams of the tested steels, and Fig. 8 displays the equivalent circuit developed based on EIS measurement data. In the circuit, R_s represents solution resistance, R_{ct} is charge transfer resistance, and CPE_{dl} signifies nonideal capacitive behavior (caused by the inhomogeneity of conductance and adsorption reactions) between metal and solution interface [30]. Table 2 presents the electrochemical parameters for the equivalent circuit. Y represents constant phase angle element (CPE) admittance (it reflects the area of reactive surface as well as the extent of rust layer permeated by the corrosive solution), n signifies CPE exponent (it indicates capacitor dispersion) and its value is no more than 1 [31], and CPE_{pl} and R_{pl} respectively are the capacitance and the resistance of the protective layer.

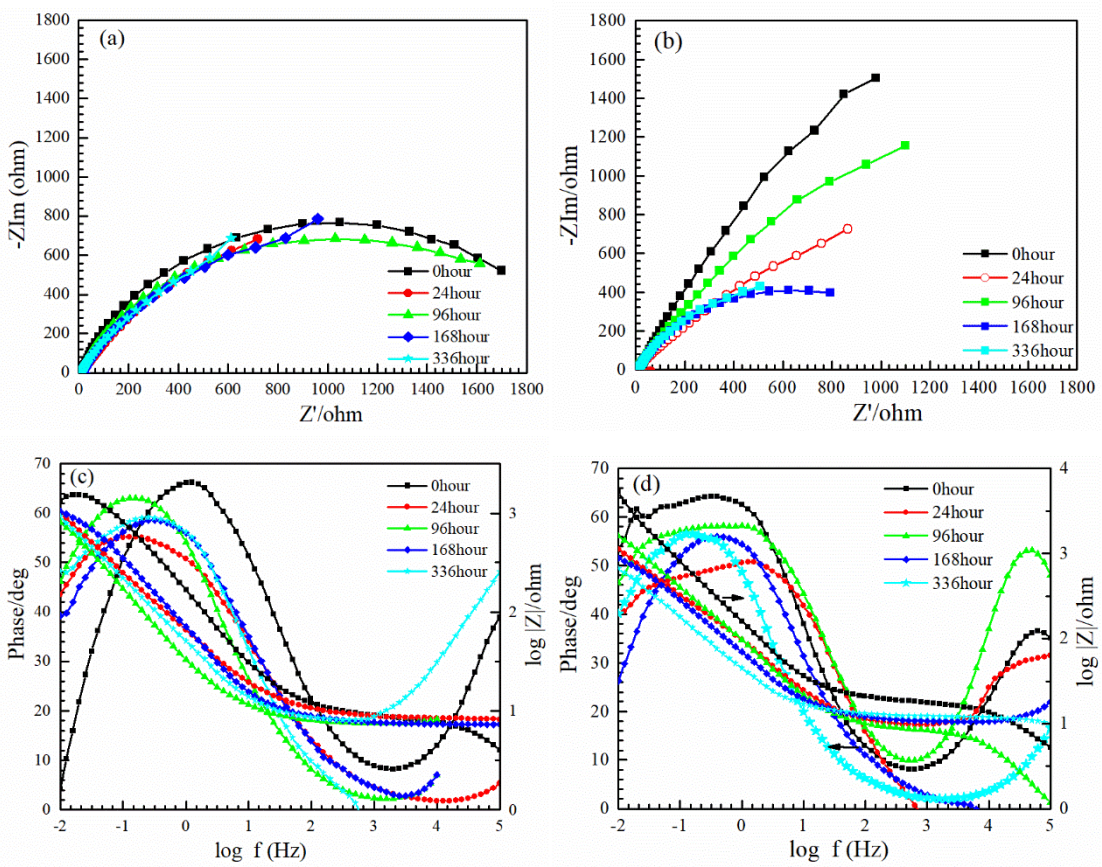

Figure 7. (a) Nyquist curves of air-cooled steel samples, (b) Nyquist curves of directly quenched steels, (c) bode/phase angle vs. frequency diagrams for air-cooled steels, and (d) bode/phase angle vs. frequency diagrams for directly quenched specimens

The presence of a small impedance, which generally reflects solution resistance at higher frequencies, can be noticed in the Nyquist curves of Figs. 7(a) and 7(b). The values of R_s were found to be less than 10 Ω, and at lower frequencies, impedance was closely related to polarized resistance [32]. The impedance arcs of AC and DQ samples manifested a decreasing trend with the extension of immersion period (Figs. 7(c) and 7(d)), whereas the values of R_{ct} started to decrease gradually.

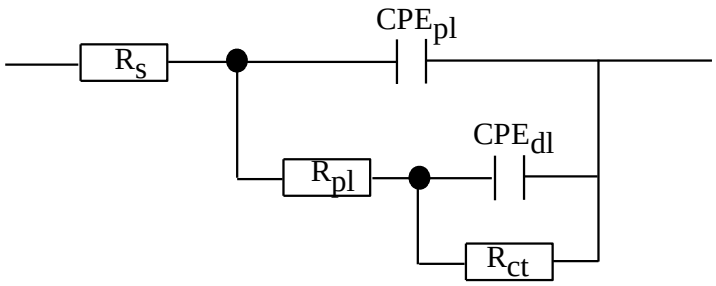

Figure 8. Equivalent circuit based on EIS measurement data

Table 2. Characteristic parameters obtained from EIS measurements for both AC and DQ steel samples

Time	R_s	CPE_{pl}		R_{pl}	CPE_{dl}		R_{ct}
		n_{pl}	Y_{pl}		n_{pl}	Y_{pl}	
AC-0 h	8.17	0.67	20.13e-3	9.35	0.78	1.43e-3	2299
AC-24 h	9.16	0.65	20.87e-3	3.38	0.64	2.30e-3	4055
AC-96 h	9.08	0.58	5.19e-3	8.59	0.64	5.20e-3	4786
AC-168 h	9.022	0.97	32.0e-3	3.87	0.69	3.89e-3	2811
AC-336 h	8.89	0.80	5.58e-3	15.30	0.57	2.10e-3	2695
DQ-0 h	8.75	0.71	17.0e-3	17.23	0.76	1.66e-3	9873
DQ-24 h	9.55	0.75	2.33e-3	17.70	0.65	3.11e-3	2594
DQ-96 h	9.33	0.91	6.87e-3	7.58	0.69	3.26e-3	4976
DQ-168 h	9.47	0.80	4.37e-3	8.01	0.80	0.48e-3	1563
DQ-336 h	9.38	0.67	32.0e-3	22.27	0.82	7.60e-3	1359

The changes in impedance arcs radius for the air-cooled sample were not obvious, and its transfer resistance (R_{ct}) first increased from 2299 $\Omega.cm^2$ (before immersion) to 4786 $\Omega.cm^2$ (after 96-h immersion) and then dropped to 2695 $\Omega.cm^2$ (after 336-h immersion). In contrast, the impedance arcs of the directly water-quenched steel sample changed dramatically with the increasing immersion times, and its R_{ct} value decreased from 9873 $\Omega.cm^2$ (before immersion) to 2594 $\Omega.cm^2$ (after 24-h immersion). Further, due to the accumulation of corrosion products on the surface, the transfer of ions was blocked; thus, the transfer resistance of the directly quenched sample increased to 4976 $\Omega.cm^2$ after 96-h immersion, and once the dynamic balance between corrosion speed and ion transfer speed was disturbed, the value of transfer resistance decreased rapidly to 1359 $\Omega.cm^2$ after 336-h immersion. The height of phase angle at the low-frequency region decreased initially and then increased with the prolonged immersion time (Figs. 7(c) and 7(d)), which confirms the variation in current density through both surface protective layer and corrosion product layer. The corrosion product layer accumulated on the DQ sample surface was loose and not uniform. With the extension of immersion period, more corrosion products covered the surface, and the corrosion product layer acted as an insulator for the matrix against aggressive ions or atoms. However, after 336-h immersion, the maximum impedance peak intensity started to decrease gradually, which signifies that the corrosion product layer lost its insulating effect and expedited the corrosive reaction [33].

3.4 Surface characterization

Fig. 9 displays the surface morphologies of AC and DQ steel specimens immersed in artificial NaCl solution for 24, 96, and 336 h. During early immersion stages, the air-cooled sample was covered with a small number of corrosion products (Figs. 9(a) and 9(d)); hence, when the protective layer was destroyed, the steel matrix started to be eroded and some pitting holes were formed on the surface. After

96-h immersion, a sheet of loose corrosion products and some pitting holes covered the surface (Figs. 9(b) and 9(e)). With the further extension in immersion time, the corrosion reaction became more severe, and more corrosion products accumulated on the surface. Once the accumulated corrosion products were removed, the scattering of corrosion holes was noticed on the surface (Figs. 9(c) and 9(f)). After 24-h immersion, as compared to the air-cooled specimen, less number of corrosion products was formed on the surface of the directly water-quenched sample (Figs. 9(g) and 9(j)). The corrosion layer was uniform, and some bigger and deeper pitting holes (as compared to the air-cooled specimen) were developed on the surface after 96-h immersion (Figs. 9(h–l)).

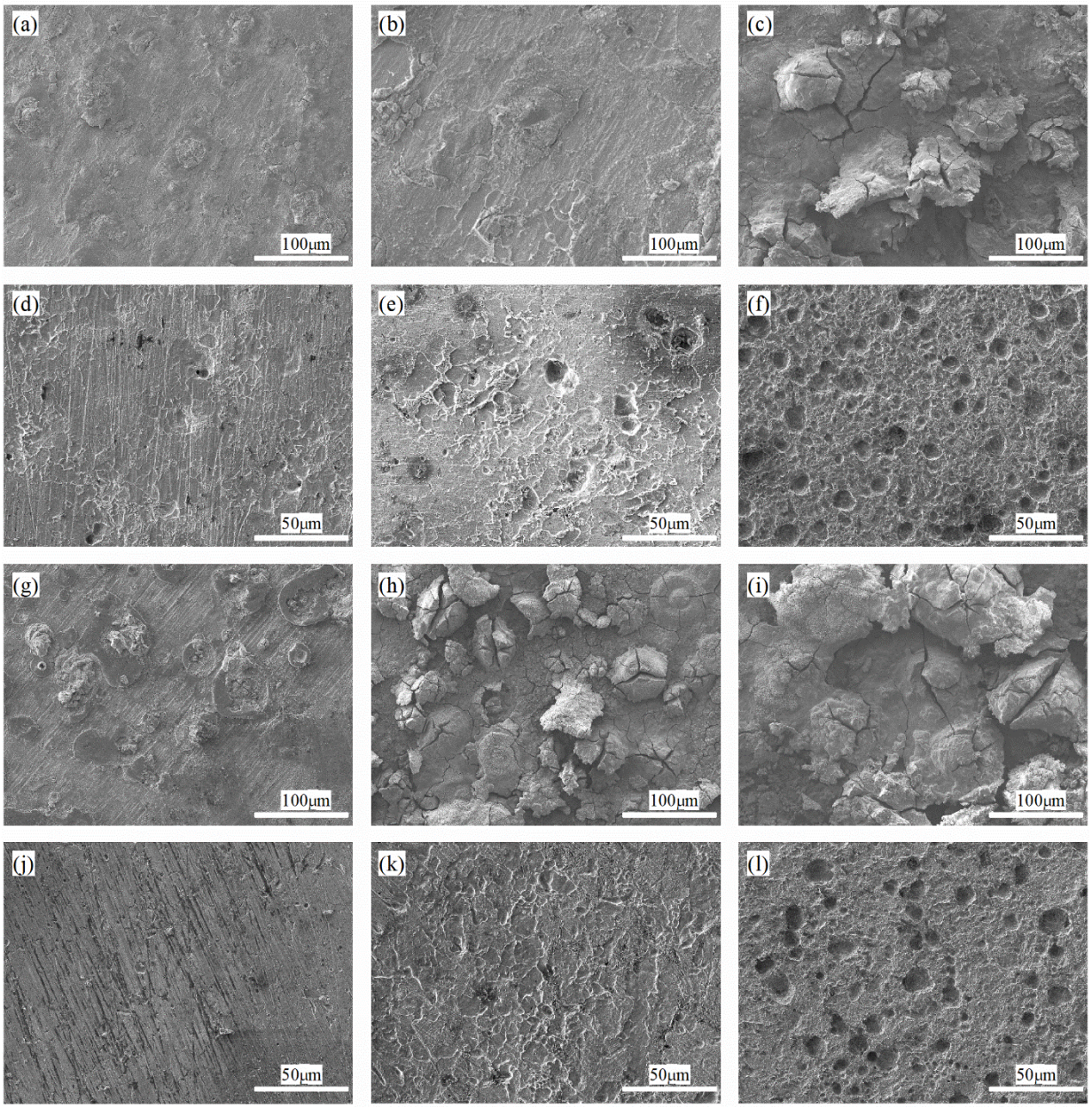

Figure 9. SEM morphologies of corrosion product layers formed on the surfaces of AC and DQ samples after (a, d, g, j) 24-h immersion, (b, e, h, k) 96-h immersion, and (c, f, i, l) 336-h immersion

Fig. 10(a) exhibits the surface of the air-cooled sample after 24-h immersion. After the removal

of corrosion products, the occurrence of uniform corrosion, pitting corrosion, and intergranular corrosion was noticed (Fig. 10(c)), and pitting holes mainly appeared in the adjacent areas of pearlites and ferrites.

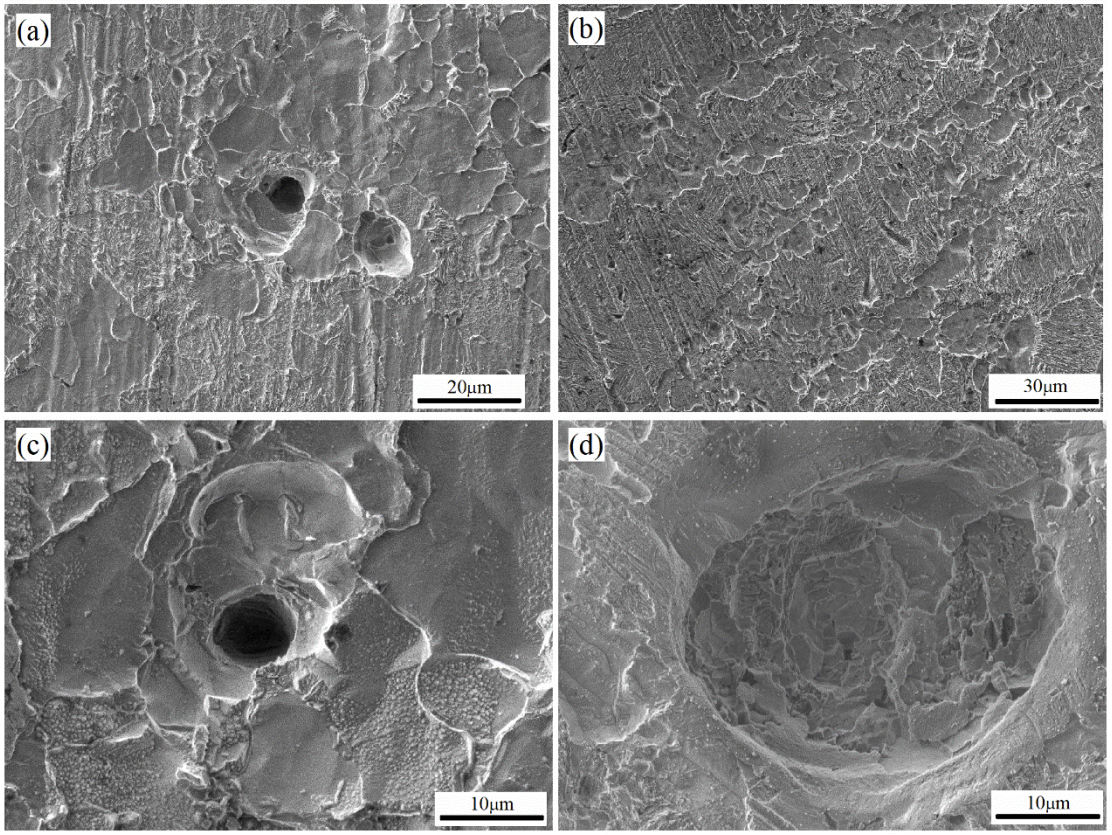

Figure 10. Surface morphologies of AC and DQ steel samples after the removal of corrosion products: (a)–(c) air-cooled sample after 24-h immersion, (b) directly water-quenched sample after 24-h immersion, and (d) formation of pitting corrosion holes on the surface of directly water-quenched steel after 168-h immersion

However, no pitting corrosion was observed on the surface of the directly water-quenched steel sample after 24-h immersion, and the corrosion velocity was found to be relatively uniform (Fig. 10(b)). It can be ascribed to the differences in carbon distribution in AC and DQ samples, thus leading to different corrosion potentials around grain boundaries. Further, after 168-h immersion, bigger and deeper (diameter of ~22 μm) pitting corrosion holes appeared on the surface of the DQ sample (Fig. 10(d)); however, the intergranular corrosion was not obvious.

3.5 Corrosion product analysis

The EDS data in Fig. 11(a) reveals that corrosion products were mainly composed of Fe and O elements, and the XRD data in Fig. 11(b) further identifies the phases of different corrosion products. It is discernible that lepidocrocite (γ-FeOOH), goethite (α-FeOOH), magnetite (Fe_3O_4), and hematite (Fe_2O_3) were the governing phases [34], and with the increasing immersion times, the characteristic peaks of γ-FeOOH, α-FeOOH, Fe_3O_4, and Fe_2O_3 became stronger.

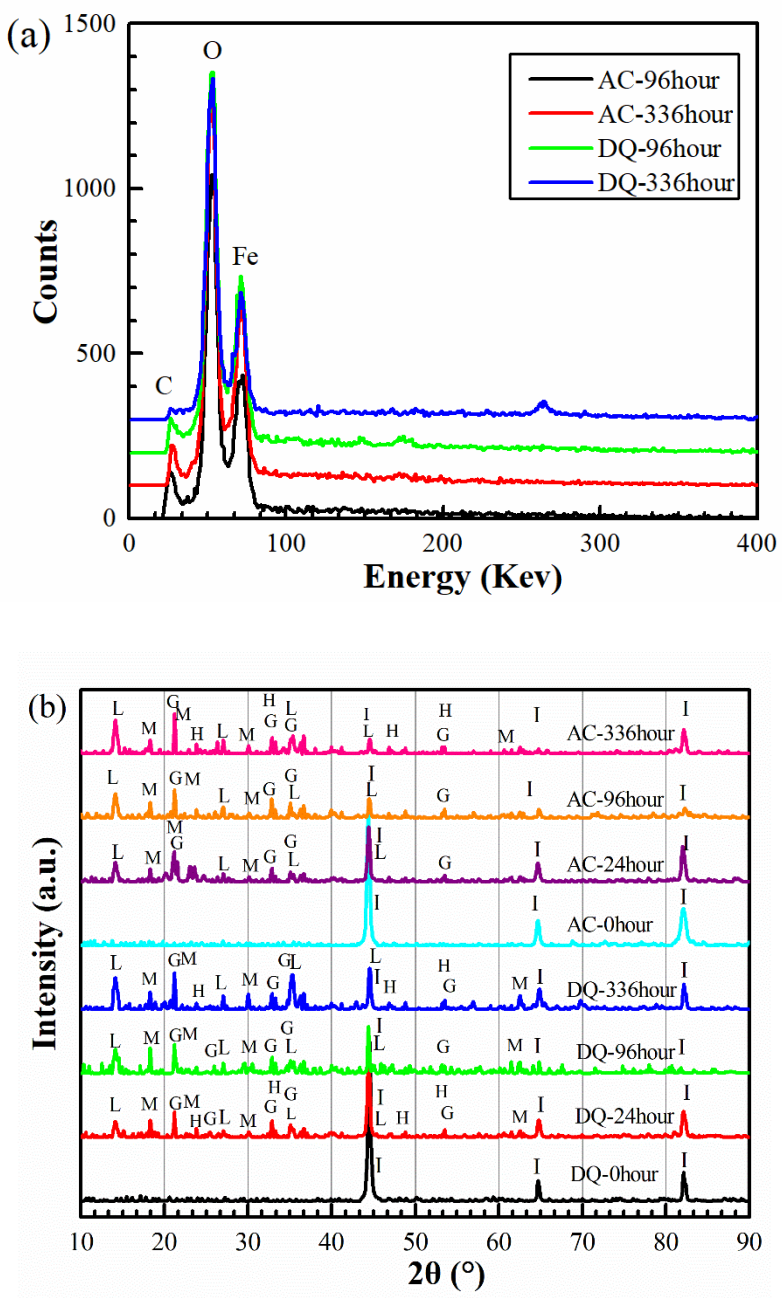

Figure 11. Identification of corrosion products by EDS and XRD: I: iron (Fe), L: lepidocrocite (γ-FeOOH), G: goethite (α-FeOOH), M: magnetite (Fe_3O_4), and H: hematite (Fe_2O_3)

3.6 Discussion

Although both AC and DQ samples possessed the same elemental composition, they yielded different microstructures and morphologies due to different cooling processes. Further, the corrosion mechanism and the corrosion velocity were analyzed through weight loss measurements (Fig. 5) and electrical-chemical methods (Figs. 6 and 7).

When the low-carbon alloy steel specimens were immersed into artificial seawater, fresh metal surfaces were exposed to NaCl solution, and consequently, corrosion started according to the following

reactions:

Anode: $Fe \rightarrow Fe^{2+} + 2e^-$ (1)

Cathode: $\frac{1}{2}O_2 + H_2O \rightarrow 2OH^- - 2e^-$ (2)

$Fe^{2+} + \frac{1}{2}O^2 + H_2O \rightarrow Fe(OH)_2$ (3)

$2Fe(OH)_2 + \frac{1}{2}O_2 \rightarrow 2FeOOH + H_2O$ (4)

Due to the diffusion of dissolved oxygen at the interface between steel and solution, a uniform corrosion reaction occurred and more corrosion products were formed on sample surfaces. On the outer layer, γ-FeOOH gradually transformed into porous α-FeOOH, which provided little protection to the substrate. However, in the inner layer, γ-FeOOH transformed into Fe_3O_4 and Fe_2O_3 (Equations 5 and 6) to form a more stable iron oxide [35] (Fig. 11(b)):

Anode: $Fe - 2e^- \rightarrow Fe^{2+}$ (5)

Cathode: $6FeOOH + 2e^- \rightarrow 2Fe_3O_4 + 2H_2O + 2OH^-$ (6)

The corrosion layer was damaged by Cl^- ions according to the following reactions:

$2Fe^{2+} + 2OH^- \rightarrow (FeOH)_2$ (7)

$(FeOH)_2 + Cl^- \rightarrow Fe(OH)^+ + Cl^- + OH^-$ (8)

Therefore, Cl^- is an efficient catalyst that provides a tunnel for aggressive dissolved ions to pass the corrosion layer and expedites the substrate corrosion and the pitting corrosion.

The corrosion process of AC and DQ samples can be explained by the phenomenological marine immersion corrosion model proposed by Melchers [36-38] (Fig. 12(a)). Phase 1 represents a short-term rupture of the formed oxide layer, and corrosion is controlled by oxygen diffusion in seawater. Phase 2 depicts a nonlinear corrosion process, which is controlled by oxygen diffusion in corrosion layers. In phase 3, corrosion is mainly controlled by anaerobic conditions related to sulfate-reducing bacteria [39,40].

Fig. 12(b) displays the corrosion process in phase 1, and corrosion is governed by the rate of oxygen accumulation on the corroding surface. However, the thickness of corrosion product layers is insufficient to control oxygen diffusion. The relation between corrosion rate and immersion time is linear [38]. Fig. 12(c) presents the nonlinear corrosion process in phase 2, where corrosion is controlled by the rate of oxygen diffusion in rust layers (with increased thickness).

The initial E_{corr} of the DQ steel sample was higher than that of the AC specimen (Figs. 6(a) and 6(b)); hence, its corrosion rate was also slower than that of the AC steel (Figs. 5(a), 5(b), and 6(c)). During the preparation of the samples, oxide films were formed on steel surfaces. The formed oxide films played a protective role in separating the corrosive solution from Fe element; hence, after 24-h immersion, corrosion rate increased significantly due to oxygen diffusion and steel surfaces were protected by corrosion product layers. However, between the immersion period of 24 and 168 h, corrosion rate decreased gradually, which indicates that the diffusion efficiency of oxygen in the solution was deteriorated by the formed rust layers.

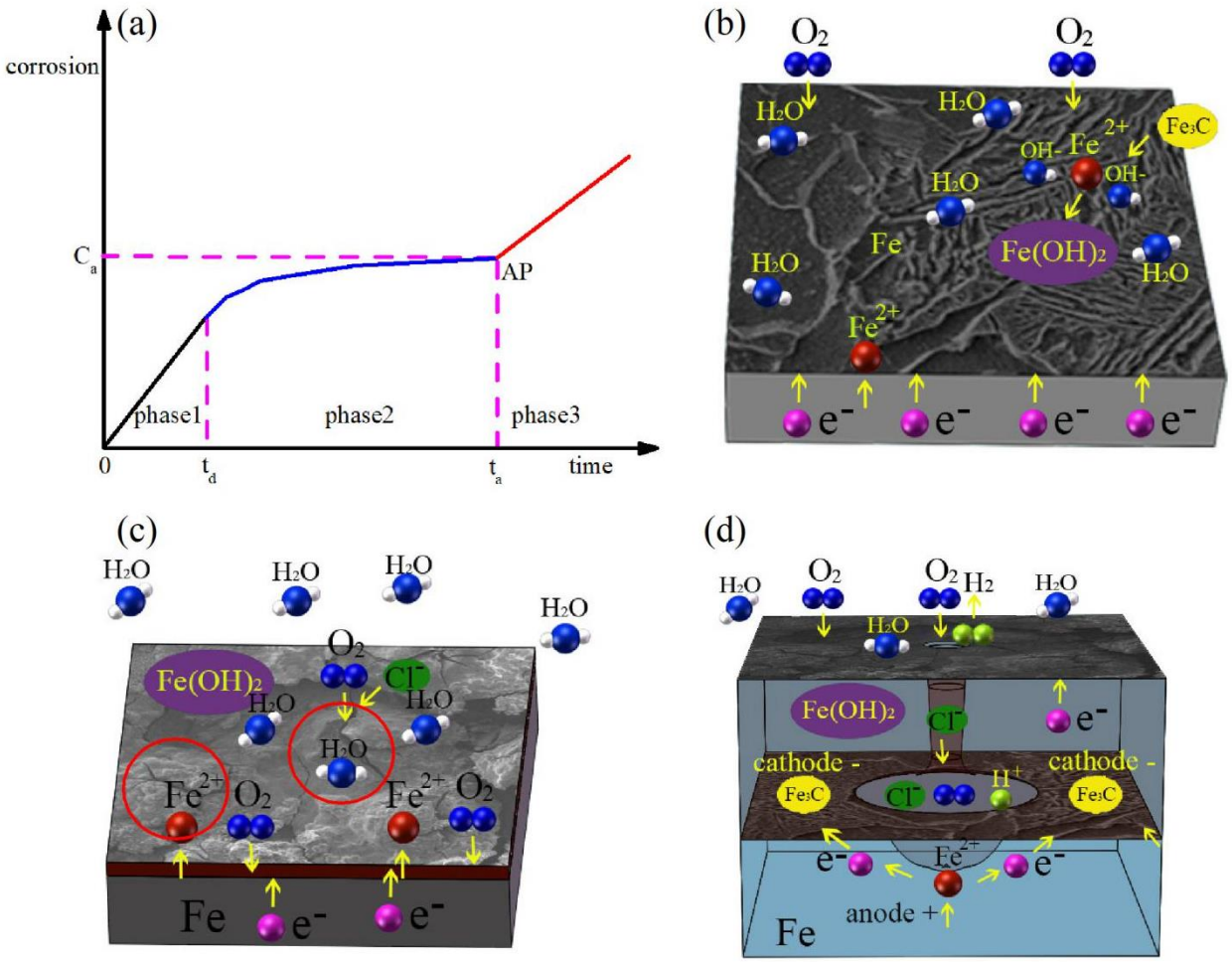

Figure 12. Schematic diagrams of corrosion process for low-temperature alloy steels in NaCl solution: (a) marine immersion corrosion model for mild steel [36]. (b) Phase 1: a short-term rupture of the formed oxide layer, and corrosion is controlled by oxygen diffusion in seawater. (c) Phase 2: a nonlinear corrosion process, which is controlled by the rate of oxygen diffusion in corrosion product layers. (d) Galvanic corrosion between the remaining cementites and ferrites (when the surface is covered with thick rust layers marked by red circles in Fig. 12(c))

Due to the accumulation of corrosion products, sample surfaces were separated by corrosion layers (Fig. 12(c)). During this period, a uniform corrosion mechanism was noticed (Figs. 9(d), 9(e), 9(j), 9(k)) and the corrosion process was hindered by dense rust layers (Figs. 5(b) and 6(c)).

The substrate of the DQ steel sample was attacked by three factors: internal stresses (generated during quenching process), galvanic corrosion (caused by remaining cementites), and residual stresses in corrosion layers. The EIS data in Fig. 6(b) manifests a rapid decreasing trend in impedance value, and after 336-h immersion, deeper and bigger pitting holes were formed on the surface of the DQ sample due to pitting corrosion (Fig. 9(l)). In AC steel, the fractions of pearlite and cementite were very small. The cooling speed during air-cooling process was slow; thus, no internal stresses were generated in the substrate. The EIS data in Fig. 6(a) depicts a slow change in impedance value; hence, an air-cooling process can significantly enhance the corrosion resistance behavior of low-carbon steels.

In our experiments, the samples were immersed vertically in the solution. Murkute [41] and Qu

[42] studied the corrosion behavior of carbon steels with respect to different exposure angles. Residual stresses influenced the porosities of protective corrosion layers and generated crack tunnels (Figs. 9(c), 9(h), and 9(i)); thus, pitting corrosion holes became more prone to Cl^- attack. During this process, pro-eutectoid ferrites as well as lamellar ferrites in pearlites and martensites were dissolved in the solution. Further, the increase in cementite content on steel surface increased the rate of corrosion due to galvanic effect [43,44] (Fig. 12(d)). Moreover, the cementite and the ferrite regions respectively acted as the cathode and the anode. The cementite phase caused galvanic corrosion, whereas the ferrite phase (especially near the cementite phase) led to anode dissolution.

4. CONCLUSIONS

In the afore-discussed work, the corrosion behavior of low-temperature TMCP carbon steels at different cooling speeds was investigated through weight loss, EIS, SEM, XRD, and EDS measurements, and the main inferences are depicted below.

(a) The directly water-quenched steel yielded more negative E_{corr} in 3.5% NaCl solution, and its corrosion resistance property started to deteriorate rapidly with the increasing immersion times.

(b) The corrosion of the matrix was inhibited by corrosion product layers after prolonged immersion periods; however, a slightly reverse phenomenon was noticed during the corrosion process of low-temperature carbon steels.

(c) The remaining cementites in the matrix caused galvanic corrosion and in turn, formed pitting holes. After an immersion period of 336 h, the galvanic corrosion reaction in the water-quenched sample occurred faster than that in the air-cooled sample.

ACKNOWLEDGEMENTS
The authors acknowledge the financial support of the National Key Research and Development Program (No.2016YFB0300700), National Natural Science Foundation of China (No.51701115)

References

1. V. Selyuzhenok, T. Krumpen, A. Mahoney, M. Janout, R. Gerdes, J. Geophys. *Res., C: Oceans*,120 (2015) 7791.
2. D. L.Gautier, K. J.Bird, R. R.Charpentier, A.Grantz, D.Houseknecht, W, Klett, T. R.Wandrey, C. J, *Science*, 324 (2009) 1175.
3. United States Central Intelligence Agency, *Polar Regions Atlas*, National Foreign Assessment Center, Washington, DC, 1978.
4. P. Layus, P Kah , A Zisman , M. Pirinen , S. Golosienko, *International Journal of Mechanical & Materials Engineering*, 11 (2016) 1.
5. M. Calcagnotto, D. Ponge, Y. Adachi , D. Raabe, *Proceedings of the 2nd International Symposium on Steel Science*, (2009) 195.
6. J.I. Leinonen, Acta Polytech., 44 (2004) 37.
7. I. Salvatori, La, Metall Ital., 5 (2006) 41.
8. C. H. Lee, K. T. Park, H. S. Shin, *Journal of Constructional Steel Research*, 74 (2012) 134.
9. Y. T. Shin, S. W. Kang, HW. Lee, *Mater Sci Eng* A., 434 (2006) 364.

10. M. Klein, H. Spindler, A. Luger, R. Rauch, P. Stiaszny, M. Eigelsberger, *Mater Sci Forum.*,500 (2005) 543.
11. Y. Nie, C. J. Shang, Y. You, X. C. Li, J. P. Cao, X. I He, *J Iron Steel Res Int*., 17 (2010) 63.
12. Seishi. TSUYAMA, *ISIJ International*, 55 (2015) 67.
13. X. D. Huo, L. J. Li, Z. W. Peng, S. J. Chen, *J Iron Steel Res In*t., 23 (2016) 593.
14. R. Parthiban, S. G. Chaudhury, K. C. Harikumar, *Mater Sci Eng* A., 705 (2017) 376.
15. J. Hu, L. X. Du, H. Xie, RDK Misra, *Mater Sci Eng* A., 607 (2016) 122.
16. S. H. Wang, C. C. Chiang, S. L. I. Chan, *Mater Sci Eng* A., 344 (2003) 288.
17. Mahesh C. Somani, David A. Porter, L. Pentti Karjalainen, Devesh K. Misra, *International Journal of Metallurgical Engineering*, 2 (2013) 154.
18. G. A. Thomas, J. G. Speer, D. K. Matlock, *Mater. Trans*. A., 42A (2011) 3652.
19. Y. Y. Wang, X. Sun, Y. D. Wang, X. H. Hu, H. M. Zbib, *Mater Sci Eng A.,* 607 (2014) 206.
20. Y. J. Li, D. Chen, D. Liu, J. Kang, G. Yuan, Q. J. Mao, G. D. Wang, *Mater Sci Eng* A., 732 (2018) 298.
21. X. D. Tian, Y. B. Xu, X. L. Yang, Z. Q. Liu, D. Wu, *Mater Sci Eng* A., 594 (2014) 149.
22. Hyojin. Song, Haksoo. Shin, Yongtaek. Shin, *Ocean Engineering*, 122 (2016) 278.
23. J. Mahieu, B. C. De Cooman, J. Maki, *Metall. Mater. Trans*. A., 33A (2002) 2573.
24. ASTM G1-03, ASTM International., 2003.
25. W. R. Osório, E.S. Freitas, A. Garcia, *Electrochim. Acta*., 102 (2013) 436.
26. E.O Halle, *Nature*, 173 (1954) 948.
27. D. A. Porter, K. E. Easterling, M. Sherif, *Phase Transformations in Metals and Alloys*, 1 (1942) 245.
28. S. Qu, X. Pang, Y. Wang, K. Gao, *Corros. Sci*., 75 (2013) 67.
29. J. Yang, Y Lu, Z. Guo, J. Gu, C. Gu, *Corros. Sci*., 130 (2018) 64.
30. B. Carrillo, R. Valdez, M. Zlatev, M. Stoycheva, M. Schorr, *Int. J. Corros*., 2011 (2011) 542.
31. R. Yildiz, *Corros. Sci*., 90 (2015) 544.
32. A. Nishikata, Q.J. Zhu, E. Tada, *Corros. Sci*., 87 (2014) 80.
33. K. S. Bokati, C. Dehghanian, S. Yari, *Corros. Sci*., 126 (2017) 272.
34. J. Guo, S. Yang, C. Shang, Y. Wang, X. He, *Corros. Sci.,* 51 (2009) 242.
35. Y. Y. Chen, H. J. Tzeng, L. I. Wei, L. H. Wang, J. C. Oung, H.C. Shih, *Corros. Sci*., 47 (2005) 1001.
36. R. E. Melchers, *Corrosion*., 59 (2003) 319.
37. R. E. Melchers, *Corros. Sci*., 45 (2003) 923.
38. R. E. Melchers, R. Jeffrey, *Corros. Sci.,* 47 (2005) 1678.
39. M. T. Gudze, R. E. Melchers, *Corros. Sci*., 50 (2008) 3296.
40. D. Jones, Principles and Prevention of Corrosion, seconded, Prentice-Hall, Upper Saddle River, NJ, 1996.
41. Pratik Murkute, Sanjay Choudhary, J. Ramkumar, K. Mondal, *J. Mater. Eng. Perform*., 26 (2016) 151.
42. S. P. Qu, X. L. K. W. Gao,and X. L. Pang. T. *Corrosion*., 7 2015 343.
43. X. Hao , J. Dong, IIN Etim, J. Wei , W. Ke,*Corros. Sci*., 110 (2016) 296.
44. Mariko. Kadowaki, Izumi. Muto,Yu. Sugawara, Takashi. Doi, Kaori. Kawano, and Nobuyoshi. Haraa, *J. Electrochem. Soc.*, 164 (2017) 261.